RSC Advances

PAPER

View Article Online
View Journal | View Issue

Cite this: *RSC Adv.*, 2022, **12**, 10163

Catalytic pyrolysis of coconut oil with Ni/SBA-15 for the production of bio jet fuel

Aldo Miro de Medeiros,[a] Karoline de Sousa Castro,[b] Mayara Lopes Gundim de Macêdo,[b] Aruzza Mabel de Morais Araújo,[a] Djalma Ribeiro da Silva[a] and Amanda Duarte Gondim[a]

Catalytic pyrolysis of vegetable oil is one of the potential routes to convert oil to drop-in biofuels, known as renewable hydrocarbons. In this paper, we explored catalytic pyrolysis of coconut oil using SBA-15 impregnated with Ni in proportions of 1% to 5% to produce sustainable aviation fuel. The catalysts were synthesized, calcined and then characterized by XRD, FTIR, SEM, and EDS. In order to better understand the behavior of this process, thermal and kinetic studies were carried out by thermogravimetry. The TG curves of vegetable oil with (10%) and without catalysts were obtained at heating rates of 5, 15 and 20 °C min^{-1}, in the temperature range between 30 and 600 °C. The kinetic parameters were calculated by the Ozawa–Flynn–Wall (OFW) and Kissinger–Akahira–Sunose (KAS) methods. In the kinetic study, lower heat rates promoted higher conversions and the KAS model suits the process. The results calculated for the OC sample using the two kinetic models showed an increase in the E_a energy as the conversion progressed to a certain point. Catalytic pyrolysis experiments were performed in a one-stage tubular reactor at 500 °C with a catalyst loading of 10 wt% on the basis of mass of oil. The catalyst with 5% Ni showed greater presence of hydrocarbons and greater formation of water, indicating that the deoxygenation process occurred through decarbonylation. With this, the present study was successful in the development of methodologies for obtaining hydrocarbons with a composition close to that of drop-in fuels, compared to the process carried out with vegetable oil in the absence of catalysts.

Received 10th February 2022
Accepted 14th March 2022

DOI: 10.1039/d2ra00866a

rsc.li/rsc-advances

Introduction

In recent years, air transport has evolved at an accelerated pace, given its advantages such as reduced travel time, safety and ease of commercial transactions.[1] Given this evolution, this sector, according to Díaz-Pérez and Serrano-Ruiz,[2] currently consumes about 2000 million barrels of oil per year, being classified as responsible for approximately 2% of global greenhouse gas emissions.[3] Faced with the expansion of air transport, these emissions could grow 5% each year.[4] These low emission values seem to make a negligible contribution compared to other transport sectors; however, aircraft emissions have a large global impact owing to the emission altitude.[5]

Among the greenhouse gases are carbon dioxide, methane and nitrous oxide. These gases absorb infrared radiation, which traps heat in the atmosphere, raising the greenhouse effect and resulting in global warming. This effect will result in alarming climate change, such as rising sea levels and catastrophic weather events.[6]

As a way to mitigate emissions from this sector and contribute to reducing climate change caused by this scenario, the International Civil Aviation Organization (ICAO) has set targets to limit emissions through carbon-neutral growth from 2020 and to cut the emissions in half by 2050 compared to 2005.[3,7] In this context, jet fuel from renewable sources is becoming a promising alternative to replacing this fossil fuel.[8] The positivity in the use of renewable sources is related to their high abundance on Earth, the possibility of recycling CO_2 reducing the concentration of this gas in the atmosphere, and decreasing dependence on crude oil.[9,10]

Given this scenario, several researchers have reported obtaining aviation biofuel using vegetable oils, among other biomasses, such as conducted by Lin and colleagues[11] investigating palm oil and Wagutu and collaborators[12] investigating croton, jatropha and coconut oils. Oil from coconut (*Coco nucifera*) stands out for having great potential for the production of aviation biofuel since its seed contains a high oil yield (63 to 65%) and its composition has a high proportion of fatty acids with chains in the range of C8 to C12, such as lauric acid and myristic acid, which are within the hydrocarbon range of aviation biofuels.[8,13]

To obtain biokerosene, five methods are certified by the American Society for Testing Materials (ASTM) according to the

[a]*Federal University of Rio Grande do Norte, Institute of Chemistry, Natal, RN, 59078-970, Brazil. E-mail: aldomiro_m@hotmail.com; aruzza.araujo@ufrn.br; amanda.gondim@ufrn.br*

[b]*Federal University of Rio Grande do Norte, Natal, RN, 59078-970, Brazil*

ASTM D7655 standard: iso-paraffinic synthesized kerosene (SIP), paraffinic and aromatic kerosene synthesized by the Fischer–Tropsch process (FT-SPKA), jet alcohol (ATJ), paraffinic kerosene synthesized by the Fischer–Tropsch process (FT-SPK) and paraffinic kerosene from the hydro-processing of esters and fatty acids (HEFA).[14–16] Another method that has been receiving attention is the pyrolysis process, which is a promising route for obtaining hydrocarbons from renewable raw materials, as demonstrated by Shah and collaborators.[17] However, in this technique, the bio-oil, initially, cannot be mixed directly with fossil kerosene since the high oxygen content in the raw material imparts undesirable properties to this product, such as high corrosivity and low energy density.[18] Therefore, the proposal of inserting catalysts to this process (catalytic pyrolysis) becomes viable as it aims to help remove oxygen from the bio-oil.

Soongprasit and collaborators[19] used SBA-15 for the thermo-catalytic pyrolysis of Sacha Inchi (*Plukenetia volubilis* L.) and verified high catalyst selectivity for hydrocarbons in the gasoline and diesel range. Using the catalysts SBA-15 and ZSM-5, Vu and Arbruster[20] evaluated the pyrolysis of residual vegetable oil and observed yields greater than 50% in gasoline production.

SBA-15 is a mesoporous material interconnected with silica-based micropores, with a highly ordered hexagonal structure.[21,22] Its characteristics are high surface area (<1000 $m^2 g^{-1}$), pores with a diameter ranging between 5 and 30 nm and thick structural walls.[23] In addition, this material also has properties such as thermal, mechanical and chemical resistance.[24] Given these attributes, SBA-15 has wide application as a biosensor, heavy metals adsorbent, drug distributor and catalyst.[25]

As a way to improve the aforementioned qualities of SBA-15, assist in the effective removal of oxygen from the bio-oil and improve the selectivity of obtaining certain products, the practice of inserting transition metals is viable.[26] Metals that present excellent deoxygenating activities are noble metals such as Pd, Ru and Pt,[27] however, their high costs have encouraged the use of non-noble metals such as Zn, Cu,[28] Co, Mo[29] and Ni.[30] Among these non-noble metals, nickel receives attention due to its low cost and several studies that proved its efficiency as a deoxygenating agent.[31] Wang and collaborators,[32] evaluating the pyrolysis of oleic acid in the presence of the Ni/MCM-41 catalyst, verified, through CHNO analysis, a decrease in the oxygen content from 10.66% to 5.02%. Veses and contributors[33] evaluated the deoxygenation of lignocellulosic biomass bio-oils in the presence of NiZSM-5 and found a decrease in oxygen content from 32.3% to 18.2% compared to thermal bio-oil. Oh and collaborators[34] investigated the deoxygenation activity of a certain bio-oil, and it was verified that the catalyst containing the metal reduced the oxygen content from 46.2% to 32.2%, with a degree of deoxygenation of 54.9%. To increase the knowledge of the thermal and thermo-catalytic reaction of coconut oil and to assess the applicability of catalysts to the reduction of activation energy (E_a), understanding the kinetics of this process is a crucial factor.[35,36] For this, the use of non-isothermal thermogravimetric analysis (TGA) is the most common method for determining pyrolysis characteristics and determining kinetic parameters, owing to fast and repeatable data collection.[37,38] With the TGA data, several mathematical models have been developed to describe this mechanism, such as the Kissinger–Akahira–Sunose (KAS) isoconversion model studied by Rasool and Kumar[38] in the pyrolysis of banyan (*Ficus benghalensis*) and the Ozawa–Flynn–Wall model studied by Reinehr and contributors[39] in the pyrolysis of green corn plant.[36]

In this context, the objective of this work is to apply thermal and kinetic studies to evaluate the catalytic pyrolysis of coconut oil in the presence of the catalysts Ni/SBA-15 and Ni/H-beta.

Results and discussion

Catalysts

The supports and catalysts were characterized by X-ray diffraction (XRD), Fourier transform infrared spectroscopy (FTIR), scanning electron microscopy (SEM) and energy dispersive spectroscopy (EDS).

The low- and high-angle diffractograms of the SBA-15 samples before and after the calcination process are shown in Fig. 1, as well as this support impregnated with 1% and 5% by mass of the metal Ni. In the low-angle diffractograms, it is noted that the samples presented three well-defined peaks referring to reflections in the (100), (110) and (200) planes. The presence of these peaks suggests that SBA-15 was synthesized with an ordered meso-structure and exhibits *P6mm* two-dimensional hexagonal symmetry typical of high-quality SBA-15-type material.[40,41] Comparing the non-calcined and calcined SBA-15 samples, it was noted that the peak intensities for the calcined sample were greater than those for the non-calcined sample. This is related to condensation of siloxane groups that occurs during the calcination process, which improves the structural order of the material.[42]

Regarding the calcined SBA-15 samples impregnated with different nickel percentages, it was observed that the 2θ values of the peaks referring to the reflection in the plane (100) underwent modification to lower values compared to the 2θ value (100) of the SBA-15. This behavior indicates that the interplanar distance and unit cell parameter (a_0) increased after nickel impregnation (Table 1).[42,43] According to Ghimere and

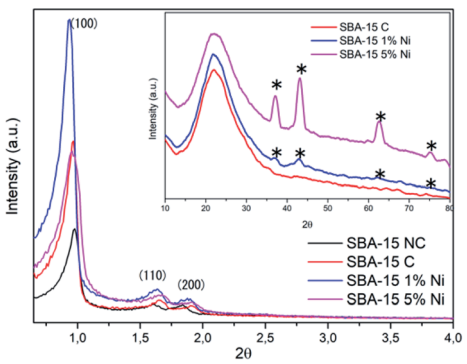

Fig. 1 Low- and high-angle diffractograms of uncalcined SBA-15 (SBA-15 NC), calcined SBA-15 (SBA-15 C), 1% Ni/SBA-15 and Ni/SBA-15. * Peaks corresponding to nickel metal.

Table 1 Peak values referring to plane reflection (100), interplanar distance (d_{100}) and unit cell parameter (a_0) of the SBA-15 C, 1% Ni/SBA-15 and 5% Ni/SBA-15 samples

Sample	2θ	d_{100}	a_0
SBA-15 C	0.9661	9.13	10.54
SBA-15 1% Ni	0.9366	9.42	10.83
SBA-15 5% Ni	0.9567	9.22	10.60

collaborators,[44] the increase in these values for nickel-impregnated samples indicates the presence of this metal in the SBA-15 since the Si–O–Ni bond length is greater than the Si–O–Si bond length, resulting in an increase in the pore size of the catalytic support. Furthermore, it is noted that these samples had the most intense d_{100} peak, with this being another point indicative of the presence of nickel, as this peak may be related to the transformation of nickel into its respective oxide after the calcination step.[45] Another point observed is the continuation of the characteristic peaks of SBA-15 even after impregnation of the metal and new calcination, suggesting that this support, after these operations, maintained the degree of ordering of its structure.[41]

With respect to high-angle diffractograms, for all samples, a large peak is observed in the region between 15° and 35°, attributed to silicon oxide, indicating the amorphous characteristic of SBA-15.[40,46] In SBA-15 samples containing 1% and 5% nickel, four peaks are observed at 2θ = 37°, 43.1°, 62.4° and 75.1°. These peaks are related to the NiO (111), (200), (220) and (311) planes, in accordance with JCPDS file no. 04-0835.[47] It is also noted that the intensities of these peaks are directly proportional to the concentration of nickel loading, thus, these intensities are higher in the 5% Ni/SBA-15 sample compared to the 1% Ni/SBA-15 sample. This same behavior was reported by Kaydouth and collaborators.[48] Thus, the presence of these peaks corresponding to the metal suggests its presence in the SBA-15.

The infrared spectra for the SBA-15 samples before and after the calcination process in the presence and absence of nickel metal are shown in Fig. 2. For all samples, the presence of a wide band is observed in the region between 3700 cm^{-1} to 3000 cm^{-1}, which comprises the Si–OH–OH stretching vibration involved in the interaction of hydrogen with water molecules adsorbed on the surface of the material.[49] A band is also present at 1623 cm^{-1}, corresponding to the bending vibration of the O–H bond of the surface hydroxyl groups and water molecules adsorbed on the silicate surface.[50] Other bands also found in all samples located at 1082 cm^{-1}, 963 cm^{-1}, 809 cm^{-1} and 458 cm^{-1} are attributed to the asymmetric vibrational elongation of the Si–O bonds of the silica network, vibration of the uncondensed silanol groups (Si–OH), the symmetric elongation vibration of the Si–O–Si bond and bending vibration of the Si–O bond of the silica lattice, respectively.[51]

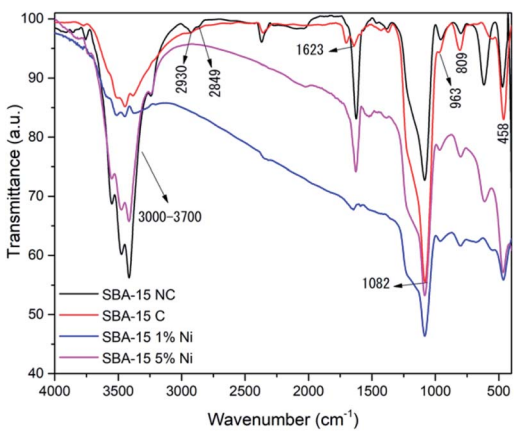

Fig. 2 FTIR spectra of uncalcined SBA-15, calcined SBA-15, 1% Ni/SBA-15 and 5% Ni/SBA-15.

However, a change in the spectra of the non-calcined and calcined SBA-15 samples was observed. In the non-calcined sample, the presence of bands at 2930 cm^{-1} and 2849 cm^{-1} was verified, which were related to the strong vibrations of the C–H bonds of the P123 organic driver.[52] The absence of these bands in the calcined sample indicated that the calcination process was efficient in its removal. Other changes were also observed in the 1082 cm^{-1} band, which was more intense in the calcined sample. The 799 cm^{-1} band in the uncalcined sample changed to 809 cm^{-1} after the calcination process due to structural contraction, as during this process the condensation of excess silanol groups occurs, reducing the concentration of these groups and, thus, resulting in vibrational band shift to a longer wavelength. Furthermore, the weakening of the intensity of the band in the region of 3700 cm^{-1} to 3000 cm^{-1} was verified; this behavior is attributed to the decrease in the concentration of silanol groups after the calcination process.[53]

Regarding the spectra of the SBA-15 samples impregnated with 1% and 5% nickel, there are subtle, but possibly significant, differences compared to the spectrum of the SBA-15 sample without metal. In the spectrum of the 1% Ni SBA-15 sample, a decrease in the intensity of the band in the region from 3700 cm^{-1} to 3000 cm^{-1} was verified, indicating the replacement of O–H bonds by O–Ni.[54] However, in the 5% Ni/SBA-15 sample, this same behavior was not observed, which may be associated with water physiosorbed on the surface of the material due to exposure to air in the sample during preparation for performing the FTIR analysis.[55] Another modification was observed in the 963 cm^{-1} band of the SBA-15 without metal. In the presence of nickel, the location of the band in the 1% Ni/SBA-15 sample was at 969 cm^{-1}, while for the 5% Ni/SBA-15 sample the band was located at 965 cm^{-1}. This event is characteristic of the metallic ion interacting with the mesoporous support structure, as reported by Bukhari and collaborators.[49] The band located at 458 cm^{-1} in the spectrum of the SBA-15 sample was shifted to 463 cm^{-1} in the spectrum of the 1% Ni/SBA-15 sample, while for the 1% Ni/SBA-15 sample the band was shifted to 466 cm-1; this behavior indicates the presence of the metal in the SBA-15.[56]

SEM analysis was performed in order to examine the morphology of the materials, as well as to verify whether the insertion of nickel metal, in the mesoporous and microporous supports, caused significant changes in the morphology of these supports. Thus, the micrographs of samples SBA-15, 1%

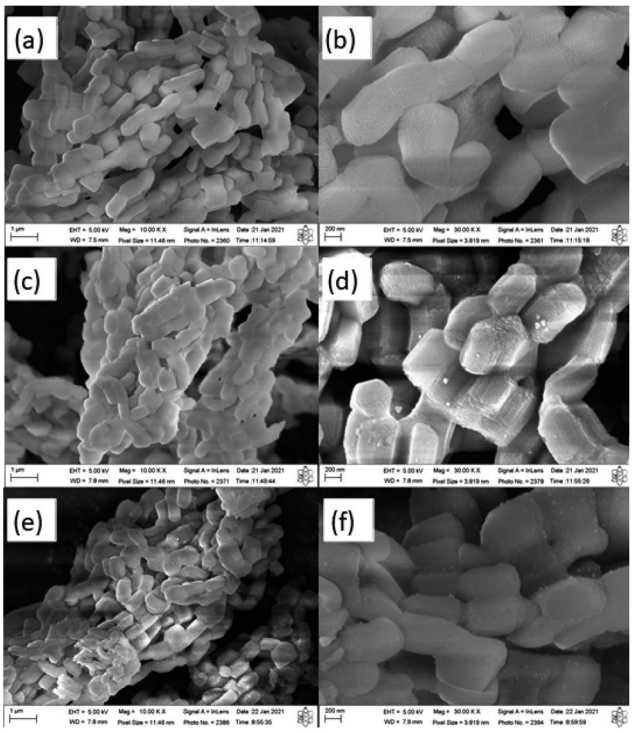

Fig. 3 Micrographs of: SBA-15 with magnifications of 100 00× (a) and 300 00× (b); 1% Ni/SBA-15 with magnifications of 100 00× (c) and 300 00× (d); and 5% Ni/SBA-15 with magnifications of 100 00× (e) and 300 00× (f).

Ni/SBA-15 and 5% Ni/SBA-15 with magnifications of 100 00× and 300 00× are presented in Fig. 3.

In the micrograph of the SBA-15 sample (Fig. 3) it is possible to observe, in general, the typical morphology of this mesoporous material: particles shaped like uniform rods, small and stacked on each other, resulting in the formation of an aggregated macrostructure.[57,58] In the high-magnification micrograph (Fig. 3(b)), it is also verified that the material has a slightly roughened surface with grooves due to the characteristic open channels of the SBA-15.[59] All of these descriptions are in line with the study by Bukhari and collaborators.[49] Looking at the micrographs with high amplification for samples 1%Ni/SBA-15 and 5% Ni/SBA-15 (Fig. 5(c–f)) the appearance of glittering particles on the support is noted, which are considered to belong to nickel metal.[60] This behavior was also reported by Erdogan and collaborators.[61] On the other hand, it is clear that there were no significant morphological changes in the catalytic support after the insertion of different percentages of nickel metal and subsequent heat treatment. This reflects the structural and thermal stability of the material.[57]

EDS analysis was used to determine the elemental composition of a certain area of the catalysts. The spectra of each sample show signals corresponding to the elements present in its composition.[62] The percentage values of the elements in the samples are listed in Table 2. Thus, for the sample 1% Ni/SBA-15, the metal was present at 1.0%, while the sample 5% Ni/SBA-15 showed the presence of the metal at 5.2%. These values are close to the target percentages to be inserted in the catalytic supports.

Table 2 Percentage of elements present in samples SBA-15, 1% Ni/SBA-15, 5% Ni/SBA-15 determined by EDS

	Elements (% de weight)			
Sample	Si	O	Al	Ni
SBA-15	53.08	46.92	0	0
1% Ni/SBA-15	52.26	46.79	0	0.96
5% Ni/SBA-15	50.79	43.95	0	5.26

Thermal and kinetic study

The tests for the thermal study were performed at three different heating rates (β) (5, 15 and 20 °C min^{-1}) in the temperature range from 30 °C to 600 °C. The graphs of the TGA and DTG curves of the OC, OC1NS, and OC5NS, samples are shown in Fig. 4. Table 3 lists the data extracted from the graphs for all samples, such as temperature range from the start to the end of the loss of sample mass, percentage of mass lost in the respective range, the maximum temperature reached, and residue at 600 °C.

Through the observations of the TGA/DTG curves of the OC sample, a single stage of mass loss can be noted, and this observation is corroborated by the presence of a single peak in the DTG, which corresponds to the predominant decomposition of the medium-chain saturated fatty acids present in the coconut oil.[63] For this sample, in the test with a heating rate of 5 °C min^{-1}, decomposition occurred between 279.9 °C and 382.8 °C, with a mass loss of 91.3%, a maximum temperature of 355.7 °C and, at the end of the process, a residue of 0.6%. For the rate of 15 °C min^{-1}, it is noted that there was an increase in the decomposition temperature range to 301.6–412.7 °C, a decrease in mass loss (91.0%), an increase in temperature

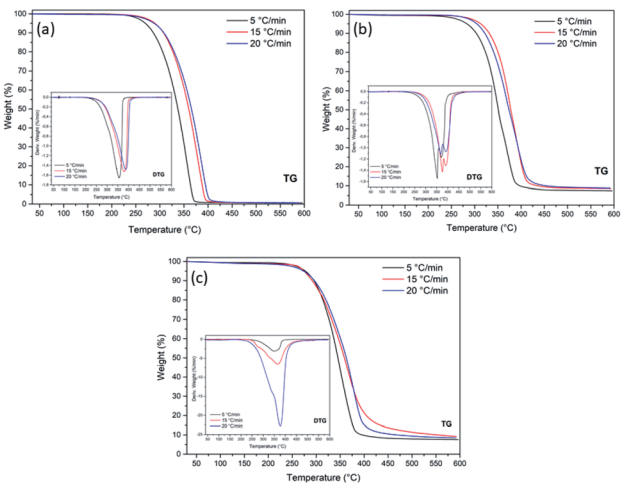

Fig. 4 TGA/DTG curves for samples (a) OC, (b) OC1NS, and (c) OC5NS, at heating rates of 5, 15, and 20 °C min^{-1}, in the temperature range from 30 °C to 600 °C.

Table 3 Loss of mass during the decomposition of coconut oil by thermal and catalytic pyrolysis

Sample	Rate (°C min^{-1})	Temp. range (°C)	Weight loss (%)	Max temp.(°C)	Residue (%)
OC	5	279.9–382.8	91.3	355.7	0.6
	15	301.6–412.8	91.0	380.5	0.7
	20	301.8–421.7	90.7	386.8	0.6
OC1NS	5	301.76–427.74	82.1	351.8	7.5
	15	329.9–455.8	81.2	375.2	8.6
	20	320.2–466.9	81.0	367.5	8.8
OC5NS	5	289.8–402.3	82.2	346.3	7.6
	15	285.8–447.7	78.0	365.5	9.2
	20	289.6–437.3	80.8	376.3	8.4

maximum (380.5 °C), and increased residue content (0.67%). At the heating rate of 20 °C min^{-1}, there is again an increase in the decomposition temperature range (301.8–421.7 °C), an increase in the maximum temperature (386.8 °C), a decrease in loss of mass (90.8%) and a decrease in the residue content (0.64%).

The presence of catalysts provided different decomposition behaviors than the sample only with vegetable oil. For example, with regard to the initial decomposition temperature, there was only a decrease in these in the OC5NS sample at the rates of 15 and 20 °C min^{-1}. Observing the final temperatures of the samples containing the catalysts, it was verified that the increase in these temperatures occurred in samples OC1NS and OC5NS for the three heating rates. This occurrence is expected when the catalyst is present, since its presence tends to slightly increase the temperature of the decomposition process, and this episode was affirmed in a study reported by Bu and collaborators.[64]

Contrary to the OC sample, not all samples containing catalyst showed an increase in the initial and final temperatures as the heating rate increased. Thus, only OC1NS exhibited such behavior at the final temperature.

Regarding the behavior of the TGA/DTG curves, it was noted that with the increase in the heating rate there were no changes in the behavior of these curves; however, there was a shift to higher maximum temperature. This behavior has been frequently observed in several works reported in the literature, such as Wako and collaborators[65] in their research on the kinetic study of the thermal degradation of rubber seed oil. According to Bouamoud and collaborators,[66] this shift is due to the temperature gradient during the reaction process, which is smaller at low heating rates and larger at a high heating rates, that is, the increase in the heating rate causes a delay in material degradation.[67] However, this behavior was not observed in the OC1NS sample, since there was a decrease in the maximum temperatures between the heating rates of 15 and 20 °C min^{-1}. The action of the catalysts in decreasing the maximum temperature, when compared to the maximum temperatures of coconut oil alone, was observed in samples OC1NS and OC5NS at all three heating rates.

With regard to the percentages of loss of mass and residues, the samples that showed a decrease and increase, respectively, of these contents as the heating rate increased were OC at the rate of 15 °C min^{-1}, OC1NS at rates of 15 and 20 °C min^{-1}, and OC5NS at the rate of 15 °C min^{-1}. This behavior is related to the partial degradation of the sample due to the thermal delay between the molecules of the material, resulting in the lower mass loss and higher residue content.[68,69]

Furthermore, in relation to the amount of mass lost and residue content, it was found that the decomposition mass of oil in the presence of catalysts was lower when compared to oil in the absence of the catalyst, following the same reasoning for the number of residues formed in the sample analyzed in the presence of catalysts, in which the amount of residue was greater. This can be related to the presence of the catalyst that is not consumed during the reaction process, its mass being constant from the beginning to the end of the reaction. Thus, decreasing the proportion of lost oil mass percentage and increasing the residue content. This episode was also observed in the catalytic cracking of sunflower oil in the presence of catalysts supported with zirconium.[70] However, the catalysts should account for at least 10% of the residual mass of the samples containing catalysts since this is the proportion of catalysts mixed with oil to perform the thermogravimetric analysis (TGA). It can be assumed that these low values may be related to the unsuccessful practice of homogenizing the mixture of oil with the catalyst at the time of carrying out the analysis.

The relationship between temperature and conversion during the degradation of coconut oil in the presence and absence of the catalysts 1% Ni/SBA-1 and 5% Ni/SBA-15 for the three heating rates (5, 15, and 20 °C min^{-1}) is shown in the graphs in Fig. 5. The conversion is counted from 0.05 to 0.9, with an increment of 0.1 where 0.05 corresponds to the beginning of the conversion (5%) and 0.9 corresponds to the end of the conversion (90%).

While observing the graphs, it can be noted that all, with the exception of the graphs corresponding to the OC1NS and OC5NS samples, they present characteristic curves relating conversion with temperature. It was noted that at the low heating rate (5 °C min^{-1}) the highest percentage conversion occurs at lower temperatures compared to the conversion temperatures for heating rates of 15 and 20 °C min^{-1}. According to Batista,[71] this occurs because at low heating rates the sample is heated longer and more uniformly than at high heating rates, thus, the conversion occurs completely and in a shorter period of time.

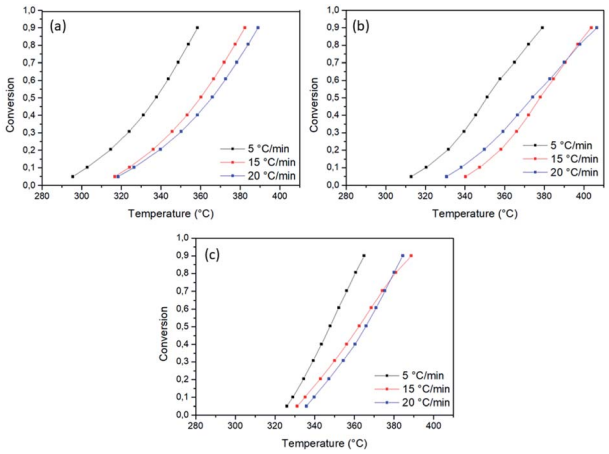

Fig. 5 Graphs of the relationship between temperature (K) and sample conversion for (a) OC, (b) OC1NS, and (c) OC5NS.

The kinetic study was based on the marked loss of mass verified in the graphs obtained from the TGA, thus, the range selected for this study was, approximately, from 230 °C to 440 °C. Fig. 6 and 7 present the graphs containing the linear regression curves of the Ozawa–Flynn–Wall (OFW) and Kissinger–Akahira–Sunose (KAS) kinetic models at the three heating rates (5, 15 and 20 °C min^{-1}) at the 10 thermal and catalytic conversion points of the samples OC, OC1NS, OC5NS. The graphs containing the linear regression curves of the kinetic OFW model are plotted using the relationship between the log of the heating rate (β) and the inverse of the temperature (K), while the graphs containing the linear regression curves of the kinetic KAS model are plotted using the relationship between the natural logarithm (ln) of the heating rate as a function of the inverse squared temperature $(\beta)/T^2$ and the inverse of the temperature (K).

It is noted that the curves of all samples for the two kinetic models present, in general, the same behavior, being arranged

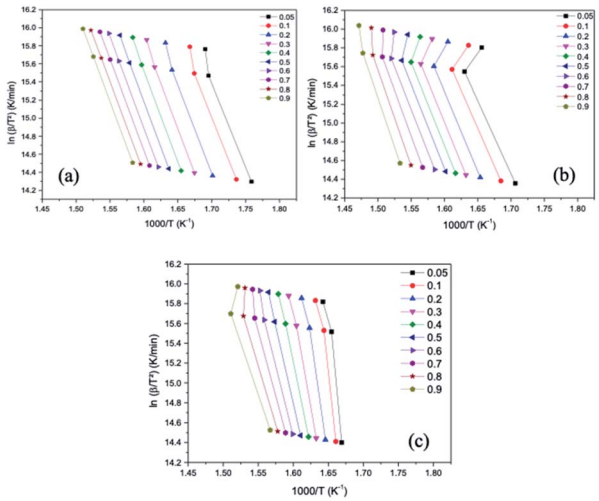

Fig. 7 Linear regression curves obtained using the Kissinger–Akahira–Sunose (KAS) model for the samples (a) OC, (b) OC1NS and (c) OC5NS.

in a parallel way and slightly distant from each other, especially for the OC sample. According to Li, Niu and Lu[72] this behavior indicates that the activation energy (E_a) in the different conversions of thermal and catalytic degradation of coconut oil follows a single mechanism. The curves of samples containing catalysts showed slight deviations, which may be related to secondary reactions caused by the presence of the catalysts.[73]

The correlation coefficients (R^2) for each conversion point, referring to the linear regression curves obtained from the OFW and KAS models of the OC, OC1NS, OC5NS samples, are shown in the graphs in Fig. 8. The correlation coefficient makes it possible to determine which of the studied kinetic models is best suited to the thermal and catalytic degradation of coconut oil. Its measurement ranges from 0 to 1, where the closer to 1, the greater the adequacy of the kinetic model in the studied process.[74]

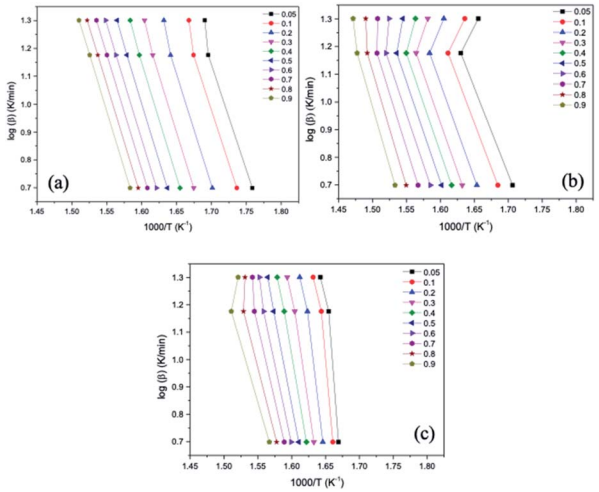

Fig. 6 Linear regression curves obtained using the Ozawa–Flynn–Wall (OFW) model for the samples (a) OC, (b) OC1NS and (c) OC5NS.

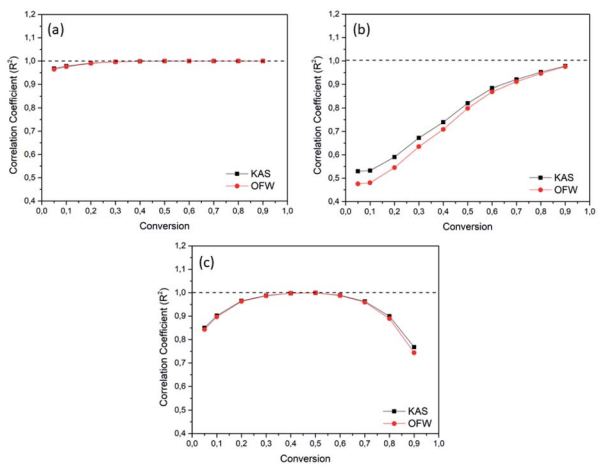

Fig. 8 Graphs of the correlation coefficient (R^2) and conversion for the Ozawa–Flynn–Wall (OFW) (red) and Kissinger–Akahira–Sunose (KAS) (black) models for the samples (a) OC, (b) OC1NS, (c) OC5NS.

It was verified that the R^2 curves for all samples presented the same behavior for both kinetic models. For the OC sample, considerable values of R^2 were found, as these values were higher than 0.9. On the other hand, OC1NS presented considerable values of R^2 above 0.9 only in the conversions from 0.05 and 0.7 to 0.9, while the OC5NS sample presented R^2 values above 0.9 only in the conversion from 0.1 to 0.7. However, it was possible to notice that for all samples the R^2 values for the KAS model were higher, indicating that this model was more suitable for the studied process. The oscillation behavior in the R^2 values for each sample, as well as the prevalence of these values for a single kinetic model, was also verified by Souza.[75]

The activation energy of the thermal and catalytic degradation of coconut oil calculated by means of the two free kinetic models is shown in Fig. 9. The E_a values calculated for the OC sample using the two kinetic models showed an increase as the conversion progressed to a certain point.[76] In the beginning, in the 0.05 conversion, the E_a corresponded to 150.78 kJ mol^{-1} for the OFW model and 370.59 kJ mol^{-1} for the KAS model, suffering a slight increase in the 0.1 conversion point and a decrease from the 0.2 point, showing an average E_a of 151.19 kJ mol^{-1} for the OFW model and an average E_a of 372.91 kJ mol^{-1} for the KAS model. This variation in energy may be related to the fact that the coconut oil decomposition reaction occurs through a chain reaction mechanism of free radicals, in which it is divided into stages of initiation, propagation, and chain termination. The initiation step requires high values of E_a, while propagation requires lower energy.[80]

The OC1NS sample showed an increase in energy in the conversion range from 0.05 to 0.5, with an E_a variation of 127.95 kJ mol^{-1} to 153.11 kJ mol^{-1} for the OFW model and a variation of 318.40 kJ mol^{-1} to 378.09 kJ mol^{-1} for the KAS model at these points, when compared with the same points in the OC samples, followed by an increase ranging from 153.36 kJ mol^{-1} to 168.42 kJ mol^{-1} for the OFW model and from 378.94 kJ mol^{-1} to 414.63 kJ mol^{-1} for the KAS model. The gradual increase in activation energy during the course of the reaction could be explained by the catalyst probably favoring the secondary cracking reaction of intermediate compounds, producing small molecules, resulting in a higher E_a in the final stage of the process.[34]

The OC5NS sample throughout the process showed E_a values higher than the energies of the sample containing only oil, showing a variation of 414.40 kJ mol^{-1} to 179.99 kJ mol^{-1} with an average of 273.56 kJ mol^{-1} for the OFW model and variation from 982.33 kJ mol^{-1} to 440.82 kJ mol^{-1} with an average of 656.82 kJ mol^{-1} for the KAS model. This event was also verified in the comparative study of the catalytic degradation of frying residues and the oil of *Pachira aquática aubl.*,[77] in which the author considered that the increase in activation energy, in the presence of the catalyst, indicates that this catalyst favors polymerization reactions, resulting in an increase in E_a.

The presence of catalysts reduced the yield of the oil fraction and increased the yield of the gaseous fraction, which may be related to favoring cracking reactions with a mechanism for the formation of radicals induced by the presence of the catalyst combined with temperature.[78] Bio-oil, water and gas yields are illustrated in Fig. 10. It is interesting to point out that the procedure carried out for the production of bio-oil did not allow the collection of the gaseous fraction, its yield being obtained by the difference between the load of initial reagents and products collected (bio-oil, solid residue and water) at the end of the process.

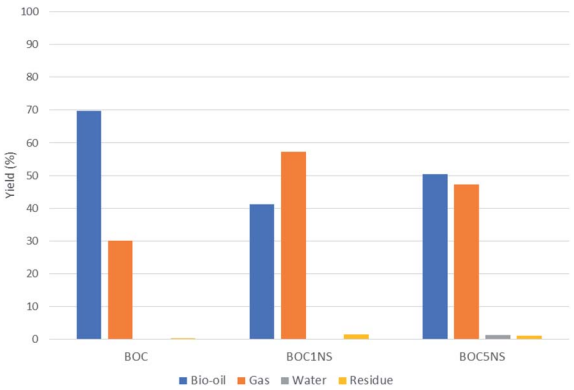

Fig. 10 Yields of products obtained from thermal and catalytic pyrolysis of coconut oil.

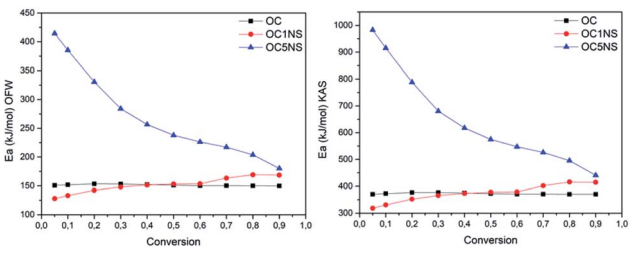

Fig. 9 Graphs of the relationship between E_a and conversion for the Ozawa–Flynn–Wall (OFW) (left) and Kissinger–Akahira–Sunose (KAS) (right) models for the OC, OC1NS, and OC5NS samples.

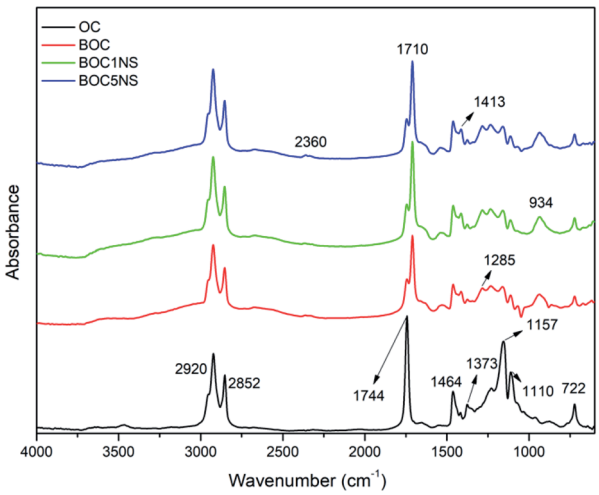

Fig. 11 Infrared spectra of coconut oil samples and bio-oils produced by thermal and catalytic processes in the presence of 1% Ni/SBA-1 and 5% Ni/SBA-15.

The catalyst with the highest Ni content, 5% Ni/SBA-15, showed a greater formation of H_2O, which indicates that there was a greater deoxygenation process when compared to thermal pyrolysis and catalytic pyrolysis with 1% Ni/SBA-15. The presence of the water indicates that the deoxygenation mechanism is primarily decarbonylation.[32,79] According to Sousa and collaborators,[80] metal has the main deoxygenation function. As already mentioned, XRD, FTIR, FTIR and SEM analyses indicated the presence of nickel metal in the microporous support for the prepared samples (1% Ni/SBA-15 and 5% Ni/SBA15), while the EDS analysis quantified it the different concentrations, corroborating the narrative of Sousa and collaborators[80] regarding the deoxygenating functionality of the metal. Thus, based on the results shown in Fig. 11 and Table 4, it can be expected that the high metal content helped in the deoxygenation of the bio-oil. The presence of metal in supports provides active sites that modify their acidic properties, leading to the improvement of these materials.[81]

The coconut oil spectrum reveals the characteristic absorption bands of vegetable oil at 2920 cm^{-1} and 2852 cm^{-1}, which correspond to the C–H stretching bands of the alkyl chain, as well as at 1744 cm^{-1} and 1464 cm^{-1}, which correspond to the stretching bands of the carbonyl functional group (C=O) of the ester bonds and flexion of the C–H bonds, respectively.[82] Other bands at 1373 cm^{-1} are related to the symmetric vibrations of the CH_3 group.[83] The bands at 1157 cm^{-1} and 1110 cm^{-1} comprise the vibrations of the C=O bond of the ester group.[84]

Paying attention to the spectra of the bio-oils samples, it is observed that there was a decrease in the intensity of the bands at 1744 cm^{-1}, 1157 cm^{-1}, and 1110 cm^{-1} both in the thermal and catalytic processes and the appearance of a band at 1710 cm^{-1}. This behavior suggests a decrease in the amount of carboxylic acid and the presence of ketones or aldehydes.[85,86]

It is noted that in the spectrum of the BOC5NS sample, all these bands have the lowest intensity when compared to the spectra of the BOC1NS and BOC sample, suggesting that the 5% H-beta catalyst favored the deoxygenation.[85]

Other bands that were present only in the bio-oil samples were 1413 cm^{-1}, 1285 cm^{-1}, 934 cm^{-1}, and 2360 cm^{-1}, which correspond to the C–H strain vibrations, stretching of C–O bonds of carboxylic acids, alcohols, aldehydes or esters, and CO_2 present in the environment, respectively.[73,86–88] The infrared spectra of bio-oil samples obtained both by thermal and catalytic processes suggest the complexity of the pyrolytic oil composition, indicating the presence of oxygenated and aliphatic organic functions. Fig. 12 presents coconut oil and bio-oils obtained through the thermal and catalytic pyrolysis process.

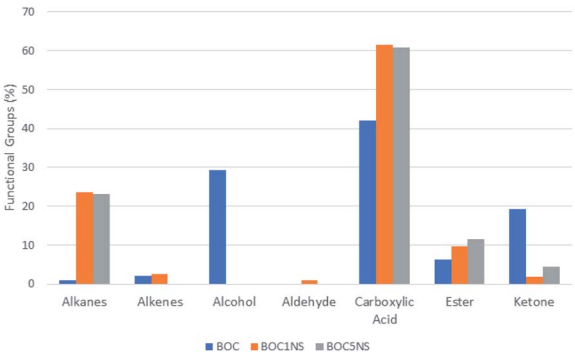

Fig. 12 Percentage of functional groups of substances present in bio-oils obtained by thermal and catalytic pyrolysis.

Table 5 lists the main substances present in the bio-oils obtained from thermal and catalytic pyrolysis, as well as the retention time (RT) and area percentage of each substance according to data from the GC-MS analysis.

According to the data presented in Tables 4 and 5, it is noted that the composition of the bio-oil obtained from the thermal process has a wide variety of substances, most of which are oxygenated compounds (96.96%), and a low amount of hydrocarbons (3.04%). The oxygenated compounds included carboxylic acids (42.17%), ketones (19.12%), esters (6.31%) and alcohols (29.36%), while the hydrocarbons were alkanes (1%) and alkenes (2.04%). The substances present in greater proportions were dodecanoic acid (35.40%) and beta-sitosterol (29.36%). Beta-sitosterol is a sterol present in vegetable oils and its presence in bio-oil indicates that there was not complete conversion to hydrocarbons. Dodecanoic acid or lauric acid is the main saturated fatty acid present in coconut oil; its presence in the bio-oil indicates that its source triglycerides were decomposed into its fatty acids and also suggests that there was not complete conversion to hydrocarbons under the reaction conditions used.[7,89]

Table 4 The wavenumbers and their attributions present in the infrared spectra of coconut oil and bio-oil samples obtained through the thermal and catalytic pyrolytic process

Sample	Wavenumber (cm^{-1})	Assignment
Coconut oil	2920–2852	Stretching bond C–H
	1744	C=O stretching
	1464	C–H bending
	1373	Symmetric vibrations of the CH_3 group
	1157–1110	Vibrations of the C=O bond
	722	Vibration of the long saturated carbon chain compounds
Bio-oils	1710	C–O stretching carboxylic acids, ketones
	1413	C–H strain vibrations
	934–1285	O–H stretching C–O(H) stretching (carboxylic acids, alcohols, aldehydes or esters)
	2360	C=O stretching (CO_2)

Table 5 Main substances present in bio-oils obtained by thermal and catalytic pyrolysis

Sample	RT (min)	Compounds	Area (%)
BOC	23.860	Decanoic acid	5.36
	31.600	Pentadecane	1.00
	36.180	Dodecanoic acid	35.40
	44.340	Tetradecanoic acid	1.41
	47.195	Decanoic acid, 2-hydroxy-1-(hydroxymethyl)ethyl ester	4.44
	52.125	Nonadecene	2.04
	55.725	Tetradecanoic acid, 2-hydroxy-1-(hydroxymethyl)ethyl ester	1.87
	56.735	8-Pentadecanone	1.95
	63.035	7-Octadecanone	2.70
	67.840	12-Tricosanone	8.36
	71.935	7-Octadecanone	6.11
	75.930	Beta-sitosterol	29.36
BOC1NS	12.695	Octanoic acid	12.76
	18.590	Tridecene	2.55
	19.075	Tridecane	11.64
	23.760	Decanoic acid	6.57
	31.590	Tetradecane	7.75
	36.025	Dodecanoic acid	42.27
	40.990	Dodecanoic acid, ethinyl ester	5.36
	41.445	Heptadecane	4.08
	41.940	Dodecanoic acid, ethinyl ester	1.98
	48.635	Myristic acid, vinyl ester	2.18
	67.845	12-Tricosanone	1.87
	71.920	10-Octadecenal	0.98
BOC5NS	12.660	Octanoic acid	12.93
	19.080	Tridecane	11.61
	23.735	Decanoic acid	5.49
	31.590	Tetradecane	7.59
	36.005	Dodecanoic acid	42.43
	40.990	Dodecanoic acid, ethinyl ester	5.00
	41.445	Heptadecane	4.02
	41.935	Dodecanoic acid, ethinyl ester	1.98
	47.175	Dodecanoic acid, 2,3-dihydroxypropyl ester	1.78
	48.625	Myristic acid, vinyl ester	2.08
	49.470	Myristic acid, vinyl ester	0.73
	67.830	12-Tricosanone	2.57
	71.915	7-Octadecanone	1.79

In the bio-oil obtained by the thermal process, the functional groups of the substances were varied, but with a low content of hydrocarbons (1%). The bio-oil obtained in the presence of the 1% Ni/SBA-15 catalyst also had a varied composition, however, with a higher content of hydrocarbons (23.47%) and carboxylic acids (61.60%). From the coconut oil pyrolysis test in the presence of the 5% Ni/SBA-15 catalyst, the bio-oil composition became less diverse. The bio-oil obtained from this test showed a higher concentration of carboxylic acids (60.85%) and a slightly lower concentration of hydrocarbons (23.22%) with relevant concentrations of esters (11.57%) and ketones (4.36%). Regarding the concentrations of hydrocarbons present in the bio-oils, it was found that 1% Ni/SBA-15 and 5% Ni/SBA-15 were selective for obtaining fractions in the range of kerosene C11–C16, obtaining 73.73%, 73.17% and 78.08%, respectively.

Experimental

Synthesis of catalytic support SBA-15

The mesoporous support SBA-15 was synthesized by the hydrothermal method described by Zhao and collaborators.[90] To obtain it, tetraethyl orthosilicate (TEOS) (Sigma Aldrich Chemistry) was used as a source of silica, Pluronic triblock copolymer (poly(ethylene oxide)–poly(propylene oxide)–poly(-ethylene oxide), (PEO20PPO70PEO20)) (P123) (Sigma Aldrich Chemistry) as the organic driver, 37% hydrochloric acid (HCl) (Synth) as the pH controller, and ethanol (EtOH) (Dynamics) and distilled water as solvents. The proportion of the molecular composition of the gel and the experimental conditions were based on the methodology described by Coutinho and collaborators.[91] Therefore, the SBA-15 gel has the following molecular composition: 1 : 0.017 : 5.7 : 193 TEOS : P123 : HCl : H_2O.

Initially, HCl was added to distilled water and then the P123 organic driver was inserted into this solution, which was kept under stirring for 2 h at 35 °C. After complete dissolution of the organic driver, TEOS was added. The reaction mixture with pH 1 was then kept under stirring for another 24 h at 35 °C. After that time, the mixture, now with the appearance of a homogeneous gel, was transferred to a Teflon autoclave and placed in an oven for 48 h at 100 °C, a step called hydrothermal treatment. Subsequently, the obtained gel was washed with a solution of 2% hydrochloric acid (HCl) in ethanol (EtOH), in order to

remove the excess of organic driver present in the pores of the SBA-15, and then filtered and dried at room temperature for 24 h; this sample was called SBA-15 NC. After the drying time, the solid was calcined at 550 °C with a heating rate of 2 °C min^{-1} for 6 h in order to eliminate the P123 organic driver; this sample was named SBA-15C.

Nickel metal impregnation on SBA-15 mesoporous support and H-beta zeolite

Nickel metal was impregnated in SBA-15 and H-beta in proportions of 1% and 5% of metal mass in relation to the support mass, using nickel nitrate hexahydrate salt [$Ni(NO_3)_2 \cdot 6H_2O$] as the metal source (Sigma Aldrich Chemistry). For the impregnation process, the incipient moisture technique was used, with the experimental conditions of this technique based on the studies by Mendonça Júnior and collaborators.[77] Hence, the salt was weighed and dissolved in a quantity of distilled water sufficient for its total dissolution (~1 mL) and later the solution was dripped onto the supports. At the end of the process, the SBA-15 and H-beta dripped with the solution were dried for 2 h at 120 °C to remove excess moisture.

Drying/calcining the SBA-15 with the nickel salt was carried out for 3 h at 450 °C with a heating rate of 5 °C min^{-1} in synthetic air, according to the procedures of Shahed and collaborators.[92] The SBA-15 catalytic supports impregnated with 1% nickel and with 5% nickel were named 1% Ni/SBA-15 and 5% Ni/SBA-15, respectively.

Catalyst characterization

The prepared catalytic supports and catalysts were characterized by XRD, FTIR, SEM, and EDS.

XRD analyses were performed using a Bruker D2Phaser diffractometer equipped with a Lynxeye detector, copper radiation (CuKα, $\lambda = 1.54$ Å) with a Ni filter, current of 10 mA and voltage of 30 kV. The SBA-15 catalytic support and its respective catalysts were analyzed with low- and high-angle scans in which the latter has the objective of evaluating the presence of the metal in the support. For the uncalcined catalytic support, only low-angle scanning was performed. Thus, low-angle scanning was performed from 0.5° to 4° with a 0.01° pitch and an acquisition time of 0.3 s. High-angle scanning was performed from 10° to 80°, with a 0.02° pitch and a 0.1 s acquisition time.

FTIR analysis was carried out using a Shimadzu IRAffinity-1 spectrometer. The samples were mixed with KBr and pressed to form a pellet. Then, the pellets corresponding to each sample were analyzed in order to obtain the spectra in the region of 400 to 4000 cm^{-1} with a resolution of 4 cm^{-1}.

SEM images were obtained using Carl Zeiss equipment, model Auriga. Before analysis, the samples were metalized with a gold monolayer for 60 s, with a current of 30 mA in a Bal-Tec metallizer, model SCD 005. Afterwards, the samples were placed on a carbon strip, and micrographs were taken with magnifications of 100 00× and 300 00×. Coupled with a scanning electron microscope, EDS was performed using a Shimadzu model Xflash Detector 410M.

Coconut oil

The renewable raw material source used to obtain the pyrolytic bio-oil was extra virgin coconut oil obtained from Empório Nuts LTDA.

Thermal and kinetic study

The thermal study was performed using data obtained from the TGA using a TA Instruments SDT Q600 V20.9 Build 20, in which the tests were performed at three heating rates (5, 15 and 20 °C min^{-1}), in the temperature range from 30 °C to 600 °C, in a nitrogen atmosphere with a flow of 50 mL min^{-1} and the samples were accommodated in an alumina crucible. In each test, an average of 15 mg of sample was used, with the catalyst at a proportion of 10% in relation to the oil mass. The tests were carried out in the oil in the presence and absence of the catalysts 1% Ni/SBA-15 and 5% Ni/SBA-15. The coconut oil sample was coded as OC, the coconut oil sample with 1% Ni/SBA-15 was coded as OC1NS and the coconut oil sample with 5% Ni/SBA-15 was coded as OC5NS. The kinetic study was carried out using the data obtained from the TGA under the same conditions used to carry out the thermal study. Activation energy (E_a) values were obtained by inserting thermogravimetric data into the Kissinger–Akahira–Sunose (KAS) and Ozawa–Flyn–Wall (OFW) kinetic models.

One of the methods used to measure the rate of thermal/thermo-catalytic decomposition or the degree of conversion of a given sample is through the loss of mass of that sample, using eqn (1):

$$\alpha = \frac{m_i m_t}{m_i m_f} \quad (1)$$

where m_i is the mass of the sample at the beginning of the reaction, m_t is the mass of the sample at a given temperature and m_f is the mass of the sample at the end of the reaction, with the extent of conversion symbolized by α.[93]

According to Almeida[94] and Ramani and collaborators,[95] the speed of a reaction depends on the extent of conversion (α), temperature (T), and time (t), and this relationship is expressed according to eqn (2):

$$\frac{d\alpha}{dt} = k(T) f(\alpha) \quad (2)$$

where $f(\alpha)$ is the reaction function and $k(T)$ is the conversion constant. This constant depends on the temperature of the mass-loss rate and is often modeled using the Arrhenius eqn (3):

$$k(T) = A \exp\left(-\frac{E_\alpha}{RT}\right) \quad (3)$$

where A is the pre-exponential factor, R is the gas constant and E is the activation energy.[96] Combining eqn (2) and (3) and considering the TGA being carried out in a non-isothermal way, the temperature becomes a function of time (t), which increases with a constant heating ratio (β). Thus, the reaction rate, in its integrated form, can be described by eqn (4):[97]

$$g(\alpha) = \int_0^T \frac{A}{\beta} \exp\left(-\frac{E_\alpha}{RT}\right) dT \quad (4)$$

According to Sokoto and collaborators[93] and Yaman,[98] the right side of the equation does not have an exact analytical solution. Therefore, several approximation methods can be used for this solution, thus forming the basis on which several equations of the integral model were derived.

One of the methods is the free or iso-conversion method, whereby this method claims that the reaction rate is just a function of temperature.[99] The term "free methods" is related to the fact that these methods provide kinetic parameters, such as activation energy (E_a), without knowledge of the reaction mechanism.[100]

Two models that are widely used in studies of pyrolysis kinetic parameters of vegetable oils are Kissinger–Akahira–Sunose (KAS) and Ozawa–Flyn–Wall (OFW). The KAS model is based on the Coats–Redfern approximations and is expressed by eqn (5):[101]

$$\ln\left(\frac{\beta}{T^2}\right) = \ln\left(\frac{AR}{E_\alpha G(\alpha)}\right) - \frac{E_a}{RT} \quad (5)$$

Activation energy values are obtained through the graph of $\ln(\beta/T^2)$ *vs.* $1/T$. The OFW model is based on Doyle approximations, being expressed by eqn (6):

$$\log(\beta) = \log\left(\frac{AE_a}{RG(\alpha)}\right) - 2.315 - 0.4567\left(\frac{E_a}{RT}\right) \quad (6)$$

Activation energy values are obtained through the graph of $\ln(\beta)$ *vs.* $1/T$ (Wako *et al.* 2017).[65]

Pyrolysis reaction

The pyrolysis procedure was performed based on the studies by Araujo and collaborators[102] using the same reactor as used in the work. To perform the thermal and catalytic pyrolysis of coconut oil, a Flyover FT-1200 fixed bed reactor was.

The procedure consisted of adding 15 g of coconut oil – when performing thermal pyrolysis – and coconut oil with 10% by weight of catalyst – when performing catalytic pyrolysis – into a boat. Then, this boat, containing the respective samples, was inserted into a reactor, and later this set was inserted into the tubular furnace in which it is equipped with a Type S thermocouple, a digital control unit, and a temperature program. At one end of the reactor, a connecting tube with a glass tap for gas connection was attached, and at the other end a condenser was attached, followed by the attachment of balloons to collect the condensed products.

Preliminary tests were carried out in order to evaluate the heating behavior of vegetable oil. Thus, the tests were performed with different ramps ranging from ambient temperature to 510 °C, with heating rates of 8 and 30 °C min^{-1}, and times of 5, 6, 8, and 10 min. Thus, based on the observations from the tests carried out and with the help of the results of the TGA, the thermal and catalytic pyrolysis of coconut oil were both carried out under an atmosphere of N_2, with a flow of approximately 100 mL min^{-1} with four heating ramp configurations. Therefore, the reaction condition of the first ramp was set to heat from ambient temperature up to 360 °C with a heating rate of 30 °C min^{-1} for 5 min. The second ramp was configured to heat from ambient temperature up to 410 °C with a heating rate of 8 °C min^{-1} for 10 min, the third ramp was configured to heat from ambient temperature up to 460 °C with a heating rate of 8 °C min^{-1} for 10 min and the fourth ramp was configured to heat from ambient temperature up to 510 °C at a heating rate 8 °C min^{-1} for 10 min. The duration of the entire process, from the beginning to the cooling of the reactor and the removal of the residue present in the boat, was approximately 4 h.

The bio-oil sample obtained from the pyrolysis process with coconut oil alone was coded as BOC, the bio-oil sample obtained from the reaction of coconut oil with the catalyst 1% Ni/SBA-15 was coded as BOC1NS, and the bio-oil sample obtained from the reaction of coconut oil with 5% Ni/SBA-15 catalyst was coded as BOC5NS.

Characterization of coconut oil and bio-oils

The functional groups of the catalytic pyrolysis products were evaluated using FTIR in the range of 400 to 4000 cm^{-1} using a Shimadzu IRAffinity-1 with an attenuated total reflectance (ATR) sensor employing a zinc selenide (ZnSe) crystal.

The identification of bio-oil compounds was carried out through GC-MS using a Shimadzu QP2010 (Kyoto, Japan). This analysis was carried out using 1 μL of the sample, under an atmosphere of helium gas with a flow rate of 1.0 mL min^{-1}, an analysis time of 82 min, a separation ratio of 100 : 1 and GC-MS interface temperature of 250 °C (injector temperature). The bio-oil was separated on a 30 cm long, 0.25 mm diameter SH-Rtx-5MS capillary column with 0.25 μm stationary phase thickness. The column pressure was maintained at 0.63 kgf cm^2, with a flow rate of 0.96 mL min^{-1} and a linear velocity of 36.1 cm s^{-1}. The chromatography oven was programmed as follows: temperature 80 °C for 5 min, followed by heating to 180 °C at a heating rate of 3 °C min^{-1}. The scheduled time was 5 min. Heating then continued until 260 °C at a heating rate of 4 °C min^{-1}. The scheduled time was 10 min. The GC-MS interface temperature was maintained at 260 °C. The detection range of the mass spectrometer was maintained between 50 and 500 m/z, the scanning interval was 0.50 s and the scanning speed was 1666 uma s^{-1}.

The pyrolysis products of the coconut oil were identified using NIST (National Institute of Technology Standards) library database software coupled to the GC-MS analysis system. The products were quantified by the standardization method (% area). With the data obtained from the library database, fractionation of the range of interest was carried out based on the % area of the peaks found.

Conclusions

The present work intensified the study of the catalytic pyrolysis of coconut oil in the production of aviation biokerosene. The characterization of the SBA-15 samples suggested an ordered mesostructured two-dimensional hexagonal symmetry of high

quality and showed that this support maintained the degree of ordering of its structure even after nickel impregnation. The thermal study showed that the increase in heating rate provided variable behaviors. However, this increase also provided an increase in the temperature range, as well as in the maximum temperature, and a decrease in mass loss. An exception was the OC1NS sample, as there was a decrease in maximum temperature between heating rates of 15 and 20 °C min^{-1}. In general, it was verified through the kinetic study that the lower heating rates provided a higher percentage conversion. This was to be expected, as in this way the reactions occur more uniformly. It was also noted that the KAS model presented higher R^2 values than the OFW model, showing that the former was better suited to the thermo-catalytic pyrolysis of coconut oil. The catalyst 5% Ni SBA-15 Ni proved to be the most efficient in reducing the activation energy (E_a) of the reaction. The pyrolysis in the presence of the catalysts under study presents a more than 20% increase in the percentage of hydrocarbons in the bio-oil and consequently a reduction of the percentage of oxygenate. For the hydrocarbons present in the bio-oils, it was found that 1% Ni/SBA-15 and 5% Ni/SBA-5 were selective in obtaining fractions in the range of kerosene (C11–C16).

Author contributions

Medeiros AM: methodology, formal analysis, investigation, writing – review & editing, Castro KS: methodology, formal analysis, Macêdo MLG: methodology, formal analysis, Araujo AMM: writing – review & editing, data curation, validation, Silva DR: conceptualization, supervision, Gondim AD: conceptualization, data curation, validation, review & editing, supervision.

Conflicts of interest

The authors declare that they have no known competing financial interests or personal relationships that could have appeared to influence the work reported in this paper.

Acknowledgements

The authors thank the Federal University of Rio Grande do Norte (UFRN), Institute of Chemistry (IQ-UFRN), Center of Primary Processing and Reuse of Produced Water and Waste (NUPPRAR-UFRN), Programa de Recursos Humanos da ANP – PRH-37/ANP and Brazilian aviation biokerosene network (RBQAV).

Notes and references

1 I. N. Santos, E. G. P. Almeida, A. L. B. Xavier, A. C. S. Barreto and J. W. Barreto, *Anais do IX*, Simpósio de Engenharia de Produção de Sergipe, 2017.
2 M. A. Díaz-Pérez and J. C. Serrano-Ruiz, *Molecules*, 2020, **25**, 802–820.
3 L. M. Souza, P. A. S. Mendes and D. A. G. Aranda, *Renewable Energy*, 2020, **149**, 1339–1351.
4 Z. Shahinuzzaman, Z. Yaakob and Y. Ahmed, *Renewable Sustainable Energy Rev.*, 2017, **77**, 1375–1384.
5 A. Al-Lal, A. Llamas, D. Bolonio, F. Sanz-Pérez, M. Lapuerta and L. Canoira, *Global NEST J.*, 2014, **6**, 1066–1075.
6 D. W. Kweku, O. Bismark, A. Maxwell, K. A. Desmond, K. B. Danso, E. A. Oti-Mensah, A. T. Quachie and B. B. Adormaa, *J. Sci. Res. Rep.*, 2017, **17**, 1–9.
7 I. Goulart, F. F. Barbosa and P. Bernasconi, *Esquema de redução de emissões de aviação civil internacional (Corsia/Icao): Desafios e oportunidades para o Brasil*, IDESAM, São Paulo, 2018.
8 M. Al-Muttaqii, F. Kurniawansyah, D. H. Prajitno and A. Roesyadi, *Bull. Chem. React. Eng. Catal.*, 2019, **14**, 309–319.
9 F. Yoshinaga, A. S. Santos, B. F. S. Moura and G. G. Bortoleto, *Bioenergia em Revista: Diálogos*, 2020, **10**, 73–91.
10 Z. Eller, Z. Varga and J. Hancsók, *Energy Fuels*, 2019, **33**, 6444–6453.
11 C. Lin, Y. Chen and W. Wang, *Fuel*, 2020, **260**, 116345.
12 A. Q. Wagutu, S. C. Chhabra, C. L. Thoruwa, T. F. Thoruwa and R. L. A. Mahunnah, *Bull. Chem. Soc. Ethiop.*, 2009, **23**, 359–370.
13 N. Saifuddin, F. A. Siti, P. Kumaran, N. Pei-Juan and P. Priathashini, *Environ. Earth Sci.*, 2016, **32**, 012039.
14 K. S. Castro, L. F. M. Costa, V. J. Fernandes Junior, R. O. Lima, A. M. M. Araujo, M. C. S. Sant'anna, N. A. Santos and A. D. Gondim, *R. Soc. Chem. Adv.*, 2021, **11**, 555–564.
15 A. P. P. Pires, Y. Han, J. Kramlich and M. Garcia-Perez, *BioResources*, 2018, **13**, 2632–2657.
16 U. Neuling and M. Kaltschmitt, *Biomass Convers. Biorefin.*, 2015, **5**, 367–385.
17 Z. Shah, R. C. Veses, J. C. P. Vaghetti, V. D. A. Amorim and R. Silva, *Int. J. Green Energy*, 2019, **16**, 350–360.
18 M. Ajam, C. Woolard and C. L. Wiljoen, *Proceedings of the 13° international conference on stability, Handling use of liquid fuels (IASH2013)*, Rhodes, Greece, 2013, pp. 6–10.
19 C. Soongprasat, D. Aht-Ong, V. Srichroenchaikul, S. Vichaphund and D. Atong, *Catalysts*, 2020, **10**, 1031–1050.
20 X. H. Vu and U. Armbruster, *React. Kinet., Mech. Catal.*, 2018, **125**, 381–394.
21 M. Kokunesoski, J. Gulicovski, B. Matovic, M. Logar, S. K. Milonjic and B. Babic, *Mater. Chem. Phys.*, 2010, **124**, 1248–1252.
22 M. E. Adrover, M. Pedernera, B. B. Lebeau, V. Bucalá and L. Gallo, *Saudi Pharm. J.*, 2020, **28**, 15–24.
23 R. Huirache-Acuna, R. Nava, C. L. Peza-Ledesma, J. Lara-Romero, G. Alonso-Nunez, B. Pawelec and E. M. Rivera-Munoz, *Materials*, 2013, **6**, 4139–4167.
24 N. Rahmat, A. Z. Abdullah and A. R. Mohamed, *Am. J. Appl. Sci.*, 2010, **7**, 1579–1586.
25 E. Doustkhah, A. Baghban, M. Hussein, N. Assadi, R. Luque and S. Rostamnia, *Catal. Lett.*, 2019, 591–600.
26 R. A. El-Salamony, H. M. Gobara and S. A. Younis, *J. Water Process. Eng.*, 2017, **18**, 102–112.

27 S. Omar, Y. Yang and J. Wang, *Front. Chem. Sci. Eng.*, 2021, **15**, 4–17.
28 Z. He, J. Wu, B. Gao and H. He, *ACS Appl. Mater. Interfaces*, 2015, **7**, 2424–2432.
29 M. Attia, S. Farag and J. Chaouki, *Catalysts*, 2020, **10**, 1381–1409.
30 Q. Tan, Y. Cao and J. Li, *Renewable Energy*, 2020, **150**, 370–381.
31 C. C. Schmitt, K. Raffelt, A. Zimina, B. Krause, T. Otto, M. Rapp, J. Grunwaldt and N. Dahmen, *Top. Catal.*, 2018, **61**, 1769–1787.
32 F. Wang, F. Yu, Y. Wei, A. Li, S. Xu and X. Lu, *J. Anal. Appl. Pyrolysis*, 2021, **156**, 105146.
33 A. Veses, B. Puértolas, J. M. López, M. S. Callén, B. Solsona and T. García, *ACS Sustain. Chem. Eng.*, 2016, **4**, 1653–1660.
34 S. Oh, J. H. Lee, I. Choi and J. W. Choi, *Renewable Energy*, 2020, **149**, 1–10.
35 L. Wang, H. Lei, J. Liu and Q. Bu, *RSC Adv.*, 2018, **8**, 2169–2202.
36 D. O. Maia, A. M. S. Chagas, A. M. M. Araujo, A. V. Mendonça Junior, I. M. L. Ferreira, F. C. D. Lemos, A. S. Araujo and A. D. Gondim, *Thermochim. Acta*, 2018, **669**, 160–168.
37 A. Aboulkas and K. Harfi, *Oil Shale*, 2008, **25**, 426–443.
38 T. Rasool and S. Kumar, *Mater. Today: Proc.*, 2020, **21**, 2087–2095.
39 T. O. Reinehr, M. A. Ohara, M. P. O. Santos, J. L. M. Barros, P. R. S. Bittencourt, I. J. Baraldi, E. A. Silva and E. R. Zanatta, *J. Therm. Anal. Calorim.*, 2021, **143**, 3181–3192.
40 M. F. Kamaruzaman, Y. H. Taufiq-Yap and D. Derawi, *Biomass Bioenergy*, 2020, **134**, 105476.
41 L. A. Lima, A. C. Nogueira, J. J. Rodrigues and M. G. F. Rodrigues, *56° Congresso Brasileiro de Cerâmica*, 2012, 618–627.
42 A. Abd-Elbary, M. A. E. Nabarawi, D. H. Hassen and A. A. Taha, *Int. J. Pharm. Pharm. Sci.*, 2014, **6**(9), 183–191.
43 M. H. M. Husin, N. Dewayanto, J. Li and M. R. Nordin, *Adv. Environ. Biol.*, 2015, **9**(6), 6–14.
44 P. P. Ghimire, L. Zhang, U. A. Kinga, Q. Guo, B. Jiang and M. Jaroniec, *J. Mater. Chem. A*, 2019, **7**, 9618–9628.
45 N. Ozbay, A. S. Yargic, R. Z. Y. Sahin and E. Yaman, *Renewable Energy*, 2019, **140**, 633–646.
46 F. Akti and S. Balci, *J. Sci.*, 2019, **32**(1), 91–102.
47 L. A. García-Cerda, K. M. Bernal-Ramos, S. M. Mantemayor, M. A. López-Quevedo, B. R. Galindo and D. Bueno-Báques, *J. Nanomater.*, 2011, 6.
48 M. N. Kaydouth, N. E. Hassan, A. Davidson, S. Casale, H. E. Zakhem and P. Massiani, *Microporous Mesoporous Mater.*, 2016, **220**, 99–109.
49 S. N. Bukhari, C. C. Chong, L. P. The, D. N. Vo, N. Ainirazali, S. Triwahyono, A. A. Jalil and H. D. Setiabudi, *Int. J. Hydrogen Energy*, 2019, **44**, 20792–20804.
50 D. Bhuyan, M. Saikia and L. Saikia, *Microporous Mesoporous Mater.*, 2018, **256**, 39–48.
51 I. M. El-Nahhal, J. K. Salem, N. S. Tabasi, R. Hempelmann and F. S. Kodeh, *Chem. Phys. Lett.*, 2018, **691**, 211–218.
52 A. S. Araujo, S. A. Quintella and A. C. S. L. S. Coutinho, *Adsorption*, 2009, **15**, 306–311.
53 Z. Jin, X. Wang and X. Cui, *J. Mater. Sci.*, 2007, **42**, 465–471.
54 H. D. Setiabudi, C. C. Chong, S. M. Abed, L. P. The and S. Y. Chin, *J. Environ. Chem. Eng.*, 2018, **6**, 745–753.
55 F. Bérubé and S. Kaliaguine, *Microporous Mesoporous Mater.*, 2008, **115**, 469–479.
56 P. A. Cuello-P, L. Pernett-B, S. Bolíviar-S and C. Rivera-Goyco, *Prospectiva*, 2016, **14**, 13–21.
57 T. J. Siang, T. L. M. Pham, N. V. Cuong, P. T. T. Phuong, N. H. H. Phuc, Q. D. Truong and D. N. Vo, *Microporous Mesoporous Mater.*, 2018, **262**, 122–132.
58 L. B. O. Freitas, I. J. G. Bravo, W. A. A. Macedo and E. M. B. Sousa, *J. Sol-Gel Sci. Technol.*, 2016, **77**, 186–204.
59 D. M. Ferrer, J. A. M. Banda, R. S. Rodrigo, U. P. García, J. Y. V. Gómez and P. D. A. Vicente, *Int. J. Electrochem. Sci.*, 2018, **13**, 708–718.
60 J. Jian, D. Kuang, X. Wang, H. Zhou, H. Gao, W. Sun, Z. Yuan, J. Zeng, K. You and H. Luo, *Mater. Chem. Phys.*, 2020, **246**, 122814.
61 B. Erdogan, H. Arbag and N. Yasyerli, *Int. J. Hydrogen Energy*, 2018, **43**, 1396–1405.
62 J. M. Ramos, J. A. Eang, S. O. Flores, L. F. Hen, N. Nava, J. Navarrete, J. M. Domínguez and J. A. Szpunar, *Catal. Today*, 2020, **349**, 198–209.
63 K. Subramanian, *J. Pharm. Sci. Res.*, 2019, **11**, 3201–3209.
64 Q. Bu, H. Lei, M. Qian and G. Yadavalli, *RSC Adv.*, 2016, **6**, 100700–100707.
65 F. M. Wako, A. S. Reshad and V. V. Goud, *J. Therm. Anal. Calorim.*, 2017, **131**, 2157–2165.
66 R. Bouamoud, E. C. Moine, R. Mulongo-Masamba, A. E. Hamidi, M. Halim and S. Arsalane, *Pet. Sci.*, 2020, **17**, 255–267.
67 A. F. Rojas-González and J. I. Carrero-Mantilla, *Ing. Univ.*, 2015, **19**, 189–206.
68 R. K. Mishra and K. Mohanty, *Bioresour. Technol.*, 2018, **251**, 63–74.
69 K. S. Castro, *Dissertação (Mestrado em Ciência e Engenharia de Petróleo) – Programa de Pós-Graduação em Ciência e Engenharia de Petróleo*, Universidade Federal do Rio Grande do Norte, 2020.
70 A. A. L. Silva, D. S. Oliveira, F. R. D. Fernandes, A. G. D. Santos, V. P. S. Caldeira and L. D. Souza, *J. Therm. Anal. Calorim.*, 2018, **131**, 643–651.
71 A. C. M. Batista, *Dissertação (Mestrado em Ciência e Engenharia de Petróleo) – Programa de Pós-Graduação em Ciência e Engenharia de Petróleo*, Universidade Federal do Rio Grande do Norte, 2019.
72 H. Li, S. Niu and C. Lu, *Procedia Eng.*, 2017, **205**, 3711–3716.
73 A. Sun, B. Xu, A. H. Rony, S. Toan, S. Chen, K. A. M. Gasem, H. Adidharma, M. Fan and W. Xiang, *Energy Convers. Manage.*, 2017, **146**, 182–194.
74 J. L. F. Oliveira, *Tese (Doutorado em Química) – Programa de Pós-Graduação em Química*, Universidade Federal do Rio Grande do Norte, 2019.
75 T. T. Souza, *Dissertação (Mestrado em Ciência e Engenharia de Petróleo) – Programa de Pós-Graduação em Ciência e*

Engenharia de Petróleo, Universidade Federal do Rio Grande do Norte, 2019.
76 Y. Qiao, B. Wang, P. Zong, Y. Tian, F. Xu, D. Li, F. Li and Y. Tian, *Energy Convers. Manag.*, 2019, **199**, 1–10.
77 A. V. Mendonça Júnior, A. M. M. Araujo, V. J. Fernandes Junior, N. A. Santos, A. G. D. Santos and A. D. Gondim, *J. Therm. Anal. Calorim.*, 2019, **139**, 535–544.
78 G. D. Alisha, W. Trisunaryanti and A. Syoufian, *Silicon*, 2021.
79 A. Aho, A. Tokarev, P. Backman, N. Kumar, K. Eranen, M. Hupa, B. Holmbom, T. Salmi and D. Y. Murzin, *Top. Catal.*, 2011, **54**, 941–948.
80 F. P. Sousa, L. N. Silva, D. B. Rezende, L. C. A. Oliveira and V. M. D. Pasa, *Fuel*, 2018, **223**, 149–156.
81 Y. Shi, E. Xing, K. Wu, J. Wang, M. Yang and Y. Wu, *Catal.: Sci. Technol.*, 2017, **7**, 2385–2415.
82 W. H. Hoidy, M. B. Ahmad, E. A. Jaffar Al-Mulla, W. A. N. Md Zin Yunus and N. O. R. Azowa Bt Ibrahim, *Health & Environmental Research Online*, 2010, vol. 26, pp. 369–372.
83 D. Moigradean, M. A. Poiana and I. Gogoasa, *J. Agroaliment. Processes Technol.*, 2012, **18**, 272–276.
84 A. Rohman, *Int. J. Food Prop.*, 2017, **20**, 1447–1456.
85 N. M. Basir, N. A. M. Jamil and H. Hamdan, *Nanomater. Nanotechnol.*, 2021, **11**, 1–10.
86 A. Aboulkas, K. E. Harfi and A. Bouadili, *J. Mater. Process. Technol.*, 2008, **206**, 16–24.
87 T. Kraiem, A. B. Hassen, H. Belayouni and M. Jeguirim, *Environ. Sci. Pollut. Res.*, 2017, **24**, 9951–9961.
88 Y. Elkasabi, C. A. Mullen, M. A. Jackson and A. A. Boateng, *J. Anal. Appl. Pyrolysis*, 2015, **114**, 179–186.
89 S. Kurban, F. Erkoç and Ş. Erkoç, *Pharm. Biol.*, 2010, **48**, 637–642.
90 D. Zhao, Q. Huo, J. Feng, B. F. Chmelka and G. D. Stucky, *J. Am. Chem. Soc.*, 1998, **120**, 6024–6036.
91 A. C. S. L. S. Coutinho, S. A. Quintella, A. S. Araujo, J. M. F. Barros, A. M. G. Pedrosa, V. J. Fernandes Junior and M. J. B. Souza, *J. Therm. Anal. Calorim.*, 2007, **87**, 457–461.
92 G. V. Shahed, Z. Taherian, A. Khataee, F. Meshkani and Y. Orooji, *J. Ind. Eng. Chem.*, 2020, **86**, 73–80.
93 M. A. Sokoto, R. Singh, B. B. Krishna, J. Kumar and T. Bhaskar, *Heliyon*, 2016, **2**, e00172.
94 C. M. T. Almeida, E. D. V. Bruce, C. M. B. M. Barbosa, R. T. F. Frety and J. G. A. Pacheco, *XX Congresso Brasileiro de Engenharia Química*, 2014.
95 R. Ramani and J. Srivatava, *Thermochim. Acta*, 2010, **499**, 34–39.
96 A. Aboulkas, K. E. Harfi and A. Bouadili, *J. Mater. Process. Technol.*, 2008, **206**, 16–24.
97 N. Bhattaccharjee and A. B. Biswas, *Fuel*, 2020, 271.
98 S. Yaman, *Energy Convers. Manage.*, 2004, **45**, 651–671.
99 S. Vyazovkin, A. K. Burnham, J. M. Criado, L. A. Pérez-Maqueda, C. Popescu and N. Sbirrazzuoli, *Thermochim. Acta*, 2011, **520**, 1–19.
100 D. Trache, A. Abdelaziz and B. Siouani, *J. Therm. Anal. Calorim.*, 2017, **128**, 335–348.
101 F. M. Wako, A. S. Reshad and V. V. Goud, *J. Therm. Anal. Calorim.*, 2018, **131**, 2157–2165.
102 A. M. M. Araujo, R. O. Lima, A. D. Gondim, J. Diniz, L. D. Souza and A. S. Araujo, *Renewable Energy*, 2017, **101**, 900–906.